AIAA JOURNAL
Vol. 49, No. 10, October 2011

Compressible-Flow Simulations Using a New Large-Eddy Simulation/Reynolds-Averaged Navier–Stokes Model

Daniel A. Gieseking[*]
North Carolina State University, Raleigh, North Carolina 27695
Jung-Il Choi[†]
Yonsei University, Seoul 120-749, Republic of Korea
and
Jack R. Edwards[‡] and Hassan A. Hassan[*]
North Carolina State University, Raleigh, North Carolina 27695

DOI: 10.2514/1.J051001

A new hybrid large-eddy simulation/Reynolds-averaged Navier–Stokes simulation (LES/RANS) method is presented in this work. In this approach, the resolved turbulence kinetic energy, ensemble-averaged modeled turbulence kinetic energy and turbulence frequency, and time-resolved turbulence frequency are used to form an estimate of an outer-layer turbulence length scale that is nearly Reynolds-number-independent. The ratio of this outer-layer scale with an inner-layer length scale (proportional to the wall distance) is used to construct a blending function that facilitates the shift between an unsteady RANS formulation near solid surfaces and a LES formulation away from the wall. The new model is tested through simulations of compressible flat-plate boundary layers over a wide range of Reynolds numbers and Mach 2.86 flow over a smooth compression ramp. The results show that the new model predicts mean and second-moment statistics that are in good agreement with experiment and are comparable with those obtained using an earlier model (Edwards, J. R., Choi, J-I., and Boles, J. A., "Hybrid Large-Eddy/Reynolds-Averaged Navier–Stokes Simulation of a Mach-5 Compression Corner Interaction," *AIAA Journal*, Vol. 464, 2008, pp. 977–991.) which required a case-by-case calibration of a model constant.

Nomenclature

C = logarithmic law intercept
C_f = skin-friction coefficient
C_M = model constant for mixed-scale model
C_N = model constant for LES/RANS model
C_s = sharpening factor
C_μ = model constant for Menter baseline (0.09)
D = RANS-to-LES transition value
d = distance from nearest wall
d^+ = wall coordinate
F_1 = Menter baseline transition function
f, g = scaling functions
k = turbulence kinetic energy
L = domain length
l = turbulence length scale
M = Mach number
p = static pressure
Q = general quantity
q^2 = estimate of subgrid kinetic energy
Re = Reynolds number
r = recovery factor
S = magnitude of vorticity vector
s = surface coordinate
T = temperature
t = time
u = velocity vector
u_τ = friction velocity
V = primitive-variable vector
$\mathbf{V}$ = velocity vector
X = streamwise distance
x = coordinate
Y = vertical distance from lower wall
Z = spanwise distance
α_1 = model parameter for hybrid LES/RANS
β^* = model constant for Menter baseline (0.09)
Γ = blending function for LES/RANS eddy viscosity
γ = ratio of specific heats
Δ = grid size/filter width for LES model
Δt = time step
δ = boundary-layer thickness
ε = small parameter
η = ratio of wall distance to modeled Taylor microscale
κ = von Kármán constant (0.41)
λ = ratio of turbulence length scales
μ_t = dynamic eddy viscosity
ν = kinematic viscosity
ν_t = kinematic eddy viscosity
ρ = density
σ_k, σ_ω, $\sigma_{\omega 2}$ = model constants for Menter baseline
τ = characteristic time in ensemble-averaging
φ = LES/RANS model constant
χ_T = modeled form of Taylor microscale
ω = turbulence frequency

Subscripts

aw = adiabatic wall
i = ith component of vector, general index
j = jth component of vector
k = kth component of vector
k-ω = k-ω model
L = left state
N = new

Presented at the 48th Aerospace Sciences Meeting, Orlando, FL, 4–8 January 2010; received 13 October 2010; revision received 16 May 2011; accepted for publication 17 May 2011. Copyright © 2011 by the American Institute of Aeronautics and Astronautics, Inc. All rights reserved. Copies of this paper may be made for personal or internal use, on condition that the copier pay the $10.00 per-copy fee to the Copyright Clearance Center, Inc., 222 Rosewood Drive, Danvers, MA 01923; include the code 0001-1452/11 and $10.00 in correspondence with the CCC.

[*] Department of Mechanical and Aerospace Engineering.

[†] Department of Computational Science and Engineering.

[‡] Department of Mechanical and Aerospace Engineering; jredward@ncsu.edu.

o = total
R = right state
res = residence time
sgs = subgrid scale
w = at wall
∞ = freestream

Superscripts

A = average
M = monotone
m = power

Introduction

THE choice of a numerical technique to examine the structure of shock wave/turbulent boundary-layer interactions in high-speed engine configurations is one dictated by considerations of economy and fidelity to the underlying flow physics. Reynolds-averaged Navier–Stokes (RANS) methods have been widely applied to such flows, but there remain several discrepancies, such as inaccurate predictions of peak heating and separation/reattachment, that appear unresponsive to variations in the chosen turbulence model [1]. Such interactions are fundamentally unsteady at both large and small scales: local turbulence amplification due to bulk compression and shock motion contributes to high heating and fluctuating pressure loads near regions of flow separation and reattachment. A boundary layer will also undergo structural changes as a result of a shock-induced compression. Smaller, more tightly wrapped vortical structures appear following reattachment, and the velocity near the wall can be accelerated significantly by the combined effects of turbulence amplification and stream-tube contraction. An accurate prediction of such effects would appear to require a time-dependent modeling strategy, such as direct numerical simulation, large-eddy simulation (LES) or hybrid LES/RANS techniques.

While direct numerical simulation and LES are excellent tools for investigating fundamental aspects of shock/boundary-layer interactions, their utility becomes limited for interactions at higher Reynolds numbers, as the mesh resolution necessary to resolve fine-scale structures near solid surfaces can become prohibitively large. In contrast, LES/RANS strategies [2–6] seek to model the effects of near-wall turbulence using RANS concepts, thereby reducing required resolution levels immensely. Within this description, there are several variations. The original detached-eddy simulation (DES) method [2] and the more recent delayed detached-eddy simulation (DDES) extension [3] are designed to revert to an unsteady RANS description throughout the entirety of an attached turbulent boundary layer. Other techniques [4–6] seek to position the RANS-to-LES transition deep within the boundary layer so that the larger energy-containing eddies present in the outer layer may be resolved to the level that the mesh will allow.

At several institutions worldwide, both classes of LES/RANS methods are undergoing evaluation for their ability to predict shock/boundary-layer interactions. As part of the UFAST consortium [7], several groups have considered DES and DDES strategies as well as stimulated variants forced by synthetic-eddy turbulence generation at the inflow boundary for a range of oblique-shock impingement problems. The work of Garnier [8] represents one of the more complete extensions of this type. Peterson et al. [9,10] have reported the use of a similar type of stimulated DES in simulating sonic injection into a supersonic crossflow.

Over the last several years, we have developed alternative strategies for merging LES and RANS closures in such a way that the logarithmic layer (and below) is treated nominally as unsteady RANS and the outer parts of turbulent boundary layers, along with free-shear regions and regions of massive separation, are modeled through LES concepts [6,11–13]. The method must detect, in some fashion, the outer extent of the logarithmic layer and must shift the closure from unsteady RANS to LES as the boundary layer transitions from its logarithmic form to its wake form. This idea is in contrast to other efforts in wall-layer modeling using DES-based techniques [4], as these initiate the RANS-to-LES transition based primarily on the mesh resolution, without as much regard to the underlying boundary-layer structure. The LES/RANS method proposed in [6] has been applied successfully to a variety of compressible flows at high Reynolds numbers [11–13]. The major weakness of the approach is that it requires a problem-specific calibration to ensure that the time-averaged transition from RANS to LES occurs at the desired location within the boundary layer. The calibration procedure is specific to flat-plate boundary layers and is thus not general enough to handle strong departures from equilibrium. One of the purposes of this work is to generalize the procedures developed in [6] so that the problem-specific calibration can be avoided. Though successful predictions of second-moment quantities have been achieved for compressible flat-plate boundary layers using the original model [11], it is unclear whether the LES/RANS techniques correctly predict the observed amplification of Reynolds stress components that occurs in shock/boundary-layer interactions. Another objective of this work is to examine this issue through comparison of predicted second-moment statistics with available experimental data. In this paper, Mach 2.86 smooth-compression-corner experiments conducted at Princeton University [14–16] are considered. These interactions are not strong enough to separate the boundary layer, and as such, amplification mechanisms associated with separation/reattachment events and their concomitant effects on shock-system dynamics are not present. Nevertheless, other extra strain rates [17] still contribute to Reynolds stress amplification, and it is of interest to determine the ability of the current models to capture these effects.

Model Development

Original Model Description

The major focus of the paper is the development of a LES/RANS hybridization strategy that behaves similarly to the method of [6] but avoids the need for a problem-specific calibration. To illustrate the new approach, we begin by reviewing aspects of the original strategy. The original approach is designed to transition from RANS to LES at approximately the location where the boundary layer shifts from logarithmic to wakelike behavior. Menter's k-ω model [18], summarized in brief below, is used as the basis:

$$\frac{\partial(\rho k)}{\partial t} + \frac{\partial(\rho k u_j)}{\partial x_j} = \mu_t S^2 - \beta^* \rho \omega k + \frac{\partial}{\partial x_j}\left[(\mu + \sigma_k \mu_t)\frac{\partial k}{\partial x_j}\right] \quad (1)$$

$$\frac{\partial(\rho\omega)}{\partial t} + \frac{\partial(\rho\omega u_j)}{\partial x_j} = \gamma\rho S^2 - \beta\rho\omega^2 + \frac{\partial}{\partial x_j}\left[(\mu + \sigma_\omega \mu_t)\frac{\partial \omega}{\partial x_j}\right] + 2(1-F_1)\rho\sigma_{\omega 2}\frac{1}{\omega}\frac{\partial k}{\partial x_j}\frac{\partial \omega}{\partial x_j} \quad (2)$$

Here, S is defined as the magnitude of the vorticity vector for the cases presented in this report. Model constants and functions appearing in Eqs. (1) and (2) may be found in [18]. Hybridization of the above equation is accomplished simply by redefining the eddy viscosity:

$$\mu_t = \rho\left[\Gamma\frac{k}{\omega} + (1-\Gamma)\nu_{t,\mathrm{sgs}}\right] \quad (3)$$

with the subgrid eddy viscosity specified as [19]

$$\nu_{t,\mathrm{sgs}} = C_M S^{1/2}(q^2)^{1/4}\Delta^{3/2}, \qquad C_M = 0.06 \quad (4)$$

An estimate of the subgrid kinetic energy in Eq. (4) is obtained by test-filtering the resolved-scale velocity data:

$$q^2 = \tfrac{1}{2}(\tilde{u}_k - \hat{\tilde{u}}_k)^2 \quad (5)$$

The filter width is taken to be the cube root of the mesh-cell volume.

The response of the model is dictated by the blending function Γ, a time-dependent quantity that reaches a value of unity where an unsteady RANS response is desired and zero where an LES response is desired. It should be mentioned that, because of the effect of unsteady strain rates in enhancing the production of k and ω, one cannot expect that the ensemble-averaged values of k and ω will be equivalent to those obtained under steady-state assumptions (even with Γ equal to 1). In fact, the production of k is greatly enhanced by unsteady strain rates; the production of ω less so.

The blending function used in [6] is based on the ratio of the wall distance d to a modeled form of the Taylor microscale:

$$\Gamma = \frac{1}{2}\left(1 - \tanh\left[5\left(\frac{\kappa}{\sqrt{C_\mu}}\eta^2 - 1\right) - \phi\right]\right) \tag{6}$$

$$\eta = \frac{d}{\alpha_1 \chi_T} \tag{7}$$

where the Taylor microscale is defined as

$$\chi_T = \sqrt{\nu / C_\mu \omega} \tag{8}$$

The constant $\phi = \tanh^{-1}(0.98)$ shifts the balancing position (where $(\kappa/\sqrt{C_\mu})\eta^2 = 1$) from $\Gamma = 0.5$ to $\Gamma = 0.99$. It should be mentioned that the shifting parameter ϕ actually corrects for the fact that the time-averaged value for ω is larger than the RANS value because of the enhancement of turbulence production mentioned above.

The constant α_1 is chosen to locate the average LES to RANS transition position ($\Gamma = 0.99$) for equilibrium boundary layers at the point where the wake law starts to deviate from the log law. To determine α_1 for a particular inflow boundary layer, the following method is used. First, a prediction of the equilibrium boundary layer is obtained (given freestream properties, a specified wall thermal condition, and a value for the boundary-layer thickness) from Coles's law of the wall/wake along with the Van Driest transformation. An initial estimate for the outer extent of the log layer is defined by finding the value of d_w^+ such that

$$\left(\frac{1}{\kappa}\ell n(d_w^+) + C\right) \Big/ \left(\frac{u_{vd}}{u_\tau}\right) = 0.98 \tag{9}$$

The value of $d^+ = u_\tau d/\nu$ that corresponds to this value of d_w^+ is then found through the use of Walz's formula for the static temperature distribution within the boundary layer:

$$\frac{T}{T_\infty} = \frac{T_w}{T_\infty} + \frac{(T_{\mathrm{aw}} - T_w)}{T_\infty}\frac{u}{u_\infty} - r\frac{(\gamma - 1)}{2}M_\infty^2\left(\frac{u}{u_\infty}\right)^2 \tag{10}$$

The model constant is then found by the equivalence $d^+ = \alpha_1^2$, which arises from the use of inner-layer scaling arguments for k and ω. Specifically, in the logarithmic region, one has $\omega = u_\tau/(\kappa d\sqrt{C_\mu})$, where κ is the von Kármán constant, $C_\mu = 0.09$, and u_τ is the friction velocity. Substituting this into Eq. (6) and (7) in succession, one finds that

$$\frac{\kappa}{\sqrt{C_\mu}}\eta^2 = \frac{\kappa}{\sqrt{C_\mu}}\frac{C_\mu d^2\omega}{\alpha_1^2\nu} = \frac{u_\tau d}{\alpha_1^2\nu} = \frac{d^+}{\alpha_1^2} = 1 \tag{11}$$

at the balancing position. This procedure requires freestream information, the thermal state of the wall, and a target boundary-layer thickness, all of which are specific to a particular boundary layer. As such, the calibration procedure is not universal, and the constant that results must be adjusted on a case-by-case basis. Nevertheless, [11] shows that the model as described above accurately captures mean and second-moment compressible boundary-layer statistics over a wide range of Reynolds numbers, provided that the outer layer is resolved adequately (15–20 cells/boundary-layer thickness in all directions).

New Model Description

Our development of a new LES/RANS model centers on the construction of an alternative form for the blending function that does not need a problem-specific calibration. There are problems with using the Taylor microscale as a representative turbulence length scale far away from the wall. At high Reynolds numbers, outer-layer statistics (when scaled properly) should be independent of Reynolds number and thus of the molecular viscosity. What is needed is a local estimate of the outer-layer turbulence length scale (proportional to the boundary-layer thickness). Equating this value with the inner layer length scale (proportional to the wall distance) will give a reasonable estimate of the location of the outer part of the logarithmic region, and by analogy, a location where one might wish to shift the model response from RANS to LES. The difficulty is that the LES model locally supplies only inner-layer length scales (the wall distance plus viscous length scales) and the grid scale.

The turbulence transport equations may provide some outer-layer length-scale information. As one example, the length scale that is naturally determined from a k-ω model is

$$l_{k\text{-}\omega} = \frac{k^{1/2}}{C_\mu^{1/4}\omega} \tag{12}$$

This length scale approaches the inner scale κd in the logarithmic region and decays toward zero in the outer part of the boundary layer and in the viscous sublayer. Taking the ratio of $l_{k\text{-}\omega}$ to the inner scale and adding in a viscous length scale proportional to $\sqrt{\nu/\omega}$ gives a potential form for the argument of a new blending function:

$$\lambda = \frac{l_{\mathrm{outer}} + l_{\mathrm{visc}}}{l_{\mathrm{inner}}} = \frac{\sqrt{10\nu\omega + k}}{C_\mu^{1/4}\omega} \Big/ \kappa d = \frac{\sqrt{10\nu\omega + k}}{C_\mu^{1/4}\kappa d\omega} \tag{13}$$

with the constant (10) being chosen small enough so that the behavior of λ in the logarithmic and outer layers is not significantly influenced by the viscosity. The length-scale ratio λ should approach one or larger in the inner layer and should decay toward zero in the outer part of the boundary layer. The Menter k-ω model itself uses a ratio similar to $\lambda$to define its F_1 function. The DDES model [3] and its improved DDES (IDDES) extension [4] also use a similar function to separate attached boundary layers from freestream regions, and some of our earlier attempts at LES/RANS model development [20] also used this basic form. An advantage of this form is that there is a good correlation between a particular value of λ and the 50% value of Γ as determined through the original calibration procedure. Figure 1 shows this for the three boundary layers considered in [11]. A steady solution obtained from the Menter baseline (BSL) RANS model is used to provide the required data in this illustrative example. The length-scale ratio in this figure is $L_\Gamma = \lambda^2$. These results show that the 50% value of the blending function correlates approximately with a value of $L_\Gamma = 0.6$ and is nearly independent of Reynolds number.

There are several problems, however, with the direct use of λ, evaluated using instantaneous values for ν, ω, and k. First, as shown in Fig. 1, the decay rate of the function in the outer part of the boundary layer is rather slow. If the goal is to transition at the outer edge of the logarithmic region so that most of the boundary layer is modeled as a LES, then the functional form must be sharpened in some manner so that the decay rate is increased. Forms for the blending function that may be considered include

$$\Gamma = \tfrac{1}{2}(1 + \tanh[C_s(\lambda^m - D)]) \tag{14}$$

or

$$\Gamma = \frac{1}{2}\left(1 - \tanh\left[C_s\left(\frac{1}{\lambda^m} - D\right)\right]\right) \tag{15}$$

where C_s is the sharpening factor (normally greater than 5), D is the value for which $\Gamma = 0.5$ (the RANS-to-LES transition point), and m is a positive power.

The other problems are more subtle. Because the solutions for k and ω, as driven by an unsteady velocity field, are intrinsically noisy,

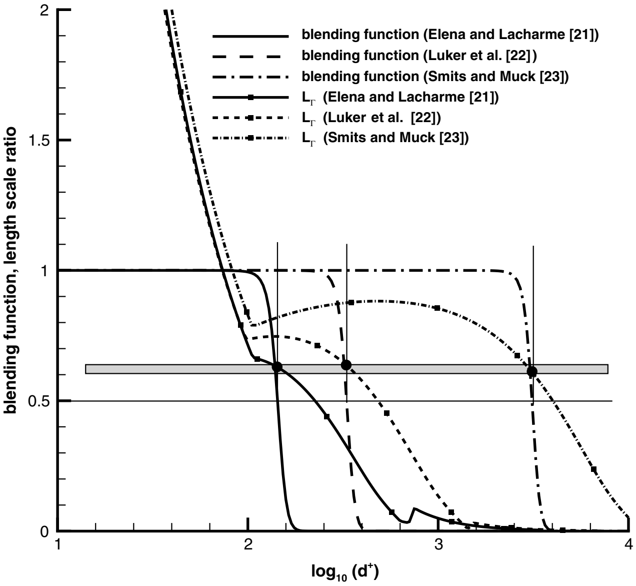

Fig. 1 Correlation between blending function and length-scale ratio for several flat-plate boundary layers (Menter BSL).

local values for the length-scale ratio may differ substantially from the time-averaged values, which themselves may differ significantly from those expected from a RANS-based analysis (as used in Fig. 1). There is also a strong coupling between the length-scale ratio, the blending function, and the transport equations themselves. The functional form for the eddy viscosity [Eq. (3)] depends on Γ, which itself depends on k and ω. The presence of Γ in the turbulence kinetic energy transport equation, in particular, induces a large damping effect on turbulence production, which causes the solution for k to be smaller than the RANS value (even where Γ may be near one locally). This can be easily seen by writing the production term as

$$\mu_t S^2 = \left[\Gamma\rho\frac{k}{\omega} + (1-\Gamma)\rho\nu_{t,\mathrm{sgs}}\right]S^2 = \rho\frac{k}{\omega}S^2 - (1-\Gamma)\rho\left(\frac{k}{\omega} - \nu_{t,\mathrm{sgs}}\right)S^2 \tag{16}$$

A consequence of this strong coupling and the diminishing of k near the RANS/LES interface is that the fixed-point solution of the LES/RANS equations (determined by the position of the time-averaged blending function within the boundary layer) may depend on the initial distribution of k. If, for example, a RANS solution is used to initialize k, the most probable response will be that the blending function stays near one throughout much of the boundary layer, meaning that turbulent fluctuations will be attenuated significantly. This is the operational mode required in DDES and related techniques, which seek to treat the entirety of an attached turbulent boundary layer as (unsteady) RANS. If the initial distribution for k is scaled so its outer-layer value is small, then the $\Gamma = 0.5$ position may stay initially near its target location, but will move toward the wall as the resolved turbulence intensity in the outer layer increases.

The original blending-function model described in the previous section avoids some of these difficulties in that it is a function of ω and not k, the former only being sensitive to the eddy viscosity through the diffusion terms and to k through the cross-derivative term in Eq. (2). Thus, the model yields stable fixed-point solutions for the time-averaged position of the blending function. However, because of the absence of outer-layer length-scale information, the original model cannot be self-adjusting and requires problem-specific calibration.

In this work, we propose a definition of the length-scale ratio that avoids some of the above issues. Instead of only using the modeled k to define the length-scale ratio, we include the resolved turbulence kinetic energy $\bar{k}_R$, which is obtained by ensemble-averaging the unsteady flowfield according to

$$\bar{\rho}\bar{k}_R = \frac{1}{2}\left(\overline{\rho u_k u_k} - \frac{\overline{\rho u_k}\,\overline{\rho u_k}}{\bar{\rho}}\right) \tag{17}$$

The length-scale ratio that results is

$$\lambda_N = C_N\frac{\sqrt{10\nu\omega + k + \bar{k}_R}}{C_\mu^{1/4}\kappa d\omega} \tag{18}$$

with C_N being a model constant. The inclusion of the resolved turbulence kinetic energy ensures that part of the outer-layer length-scale estimate is more independent of the positioning of the blending function within the boundary layer. An additional modification can be made to reduce the noise in the length-scale ratio to levels found in the original model:

$$\lambda_N = C_N\sqrt{10 + \frac{\bar{k}+\bar{k}_R}{\nu\bar{\omega}}}\frac{\sqrt{\upsilon}}{C_\mu^{1/4}\kappa d\sqrt{\omega}} \tag{19}$$

Here, we factor out the quantity $\sqrt{\nu\omega}$ and evaluate the component

$$\sqrt{10 + \frac{\bar{k}+\bar{k}_R}{\nu\bar{\omega}}}$$

using ensemble-averaged data for ω and k. The new blending function uses Eq. (19) in conjunction with Eq. (15) (with $D = 1$, $m = 2$, and C_s being a variable):

$$\Gamma_N = \frac{1}{2}\left(1 - \tanh\left[C_s\left(\frac{1}{\lambda_N^2} - 1\right)\right]\right) \tag{20}$$

In this form, it is easy to compare the new blending function with the original. One can rewrite the original form into that of Eq. (15):

$$\begin{aligned}\Gamma_o &= \frac{1}{2}\left[1 - \tanh\left(\{5 + \tanh^{-1}(0.98)\}\right.\right.\\ &\quad\times\left.\left.\left(\frac{5}{5+\tanh^{-1}(0.98)}\frac{\kappa}{C_\mu^{1/2}(\alpha_1)^2}\left(\frac{d}{\chi_T}\right)^2 - 1\right)\right]\\ &= \frac{1}{2}\left[1 - \tanh\left(7.30\left(\frac{\kappa}{1.46C_\mu^{1/2}(\alpha_1)^2}\left(\frac{d}{\chi_T}\right)^2 - 1\right)\right]\end{aligned} \tag{21}$$

Introducing the Taylor microscale into Eq. (19), one can write the new blending function as

$$\Gamma_N = \frac{1}{2}\left[1 - \tanh\left(C_s\left(\frac{1}{C_N^2\left(10 + \frac{\bar{k}_R + \langle k\rangle}{\bar{\omega}\nu}\right)}\frac{\kappa^2}{C_\mu^{1/2}}\left(\frac{d}{\lambda_T}\right)^2 - 1\right)\right] \tag{22}$$

Equating the denominators in the arguments of the original and new blending function, it is easy to see that

$$\alpha_1^2 \approx \frac{C_N^2}{1.46\kappa}\left(10 + \frac{\bar{k}_R + \langle k\rangle}{\bar{\omega}\nu}\right) \tag{23}$$

In essence, the new model replaces the problem-specific constant α_1 with a form that varies in space and also in time, as the ensemble averages may not be time-invariant and as the kinematic viscosity is a local quantity. The model constant C_N must be obtained through numerical experiments. Considering the same three compressible boundary layers as in [11] and comparing mean- and second-moment statistics with those obtained using the original model, we have determined that values of $C_N = 1.5$ to 1.6 give acceptable results. Figure 2 plots the quantity

$$\left(\frac{C_N^2}{1.46\kappa\alpha_1^2}\left(10 + \frac{\bar{k}_R + \langle k\rangle}{\bar{\omega}\nu}\right)\right)^{1/2} \tag{24}$$

versus the normalized wall distance for each of the boundary layers considered in [11]. The values of α_1 for the Elena and Lacharme [21],

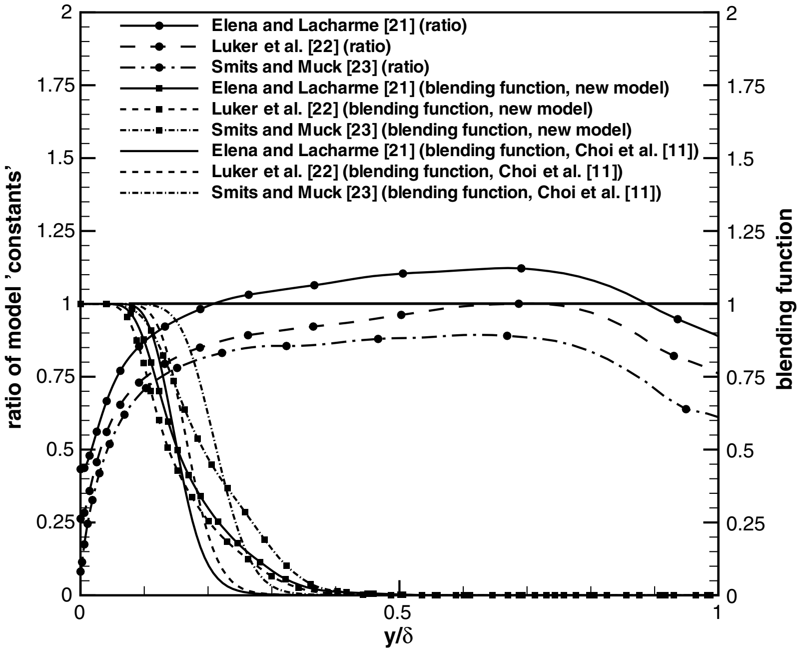

Fig. 2 Ratio of model constants and blending function distributions versus normalized wall distance for three compressible boundary layers.

Luker et al. [22], and Smits and Muck [23] experiments are 14.16, 23.22, and 75.24, respectively. The peak values for each distribution are close to unity but are lower than unity where the RANS-to-LES transition takes place ($y/\delta \sim 0.2$). Also shown in Fig. 2 are the time-averaged blending functions for the new model (with $C_N = 1.5$) and for the original model. In general, the $\Gamma = 0.5$ values are closer to the wall for the new model, but the transition zone itself ($0 < \Gamma < 1$) is broader.

An additional modification can be made to sharpen the time-averaged blending function near its 50% value. Here, we require that the subgrid-scale eddy viscosity approach the inner-layer value $kU_\tau d$ in the logarithmic region and below. This leads to an alternative form for the subgrid-scale viscosity:

$$\nu_{t,\text{sgs}} = \Gamma \kappa C_\mu^{1/4} k^{1/2} d + (1 - \Gamma)\nu_{t,\text{sgs(Eq. 4)}} \tag{25}$$

The final form of the model solves Eqs. (1) and (2), calculates the eddy viscosity field using Eq. (3), uses Eqs. (4) and (25) to determine the subgrid-scale eddy viscosity, and constructs the blending function Γ according to Eqs. (19) and (20). The model constants C_N and C_s are generally set to 1.5 and 15, respectively, though results from some variations in these constants are shown later.

Numerical Methods

The LES/RANS models are implemented into a finite volume Navier–Stokes solver written for general gas mixtures. Inviscid fluxes are discretized using a variant of the piecewise parabolic method (PPM) [24], along with Edwards's low-diffusion flux-splitting scheme [25]. The primitive-variable vector $V = [p, u, v, w, T, k, \omega]^T$ is used in the reconstruction. The initial step in the PPM reconstruction sets left and right states to

$$V^A_{L,i+1/2} = V^A_{R,i+1/2} = \tfrac{7}{12}(V_i + V_{i+1}) - \tfrac{1}{12}(V_{i+2} - V_{i-1}) \tag{26}$$

which yields a fourth-order central difference approximation on uniform meshes. Monotonicity preservation is enforced by a cell-by-cell resetting of left and right states [24], leading to final left- and right-state values ($V^M_{L/R,i+1/2}$) that are different from the averaged ones (superscript A). The amount of numerical dissipation added at a cell interface is proportional to the difference in left- and right-state values. While enforcing monotonicity preservation helps in shock-capturing, it compromises the ability of the scheme to resolve small-scale turbulent structures. One means of alleviating this problem is to blend the averaged values [Eq. (26)] with the monotonicity-preserving values so that the former is used in regions of high vorticity (boundary layers, shear layers) and the latter is used in more inviscid regions, where strong shocks might be present. A function due to Ducros et al. [26], defined at a mesh cell as

$$f = \frac{(\nabla \cdot \mathbf{V})^2}{(\nabla \cdot \mathbf{V})^2 + |\omega|^2 + \varepsilon^2}$$
$$\varepsilon = 1 \times 10^{-8} V_\infty / \max(\overline{\Delta x}, \overline{\Delta y}, \overline{\Delta z}) \tag{27}$$

has been used by several researchers [8,27,28] to provide this type of transition. Here, the divergence of velocity is compared with the vorticity value. If the latter is much larger, in shear and boundary layers, for example, the function moves toward zero, and in freestream regions near shocks, the function approaches one. At a particular cell interface $i + 1/2$, we use the function as follows:

$$V_{L,i+1/2} = V^A_{L,i+1/2} + \max(f_i, f_{i+1}, 0.1)\left(V^M_{L,i+1/2} - V^A_{L,i+1/2}\right)$$
$$V_{R,i+1/2} = V^A_{R,i+1/2} + \max(f_i, f_{i+1}, 0.1)\left(V^M_{R,i+1/2} - V^A_{R,i+1/2}\right) \tag{28}$$

The calculations described later use this scheme, termed LD-PPM, for low-dissipation PPM. Viscous and diffusive terms appearing in the equation system are discretized using second-order central differences.

Turbulent fluctuations are sustained through application of a recycling/rescaling strategy described in [6,11]. This method superimposes fluid-property fluctuations upon a baseline inflow profile determined from a RANS solution. A Klebanoff-type intermittency function is used to prevent recycled fluctuations from influencing freestream regions, and the entire recycle plane is shifted at every time step in the spanwise direction by a randomized fraction of the incoming boundary-layer thickness to inhibit the fixing of positions of longitudinal vortical structures over time. As shown in [29], this procedure does not affect turbulent statistics, which are obtained by time- and span-averaging the instantaneous data. All of the cases presented in this paper employ periodic boundary conditions in the spanwise direction, and the recycle plane is located 7.5 boundary-layer thicknesses downstream of the inflow plane.

Initialization, Time Advancement, and Ensemble-Averaging

All cases described subsequently are initialized with a steady RANS Menter BSL solution, onto which a rescaled fluctuation field from an earlier calculation is superimposed in the flat-plate region. The initial values for the turbulence variables (k, ω, F_1) are not adjusted from the RANS values. A dual-time-stepping implicit method is used to advance the equations in time. At each time step, a Crank–Nicholson discretization of the equations is solved to a prescribed tolerance using a subiteration procedure. The matrix system resulting from the linearization of the equation system is approximately solved using a planar relaxation procedure at each subiteration. Following a period of about five flow-through times to remove initial transients, time- and span-averaged statistics were collected over a minimum of seven flow-through times. The computational time step ranged from 0.25–0.4 μs, with the differences in time step being related to variations in the mesh sizes.

An issue in the implementation of the new model is the use of ensemble-averaging to compute both the resolved turbulence kinetic energy and smoother forms of the modeled turbulence kinetic energy and turbulence frequency. Ensemble-averaging in this work implies time-averaging, as averaging over a homogeneous direction may not be possible in more complicated 3-D flows. As the LES/RANS calculations are initialized from a RANS basic state, the resolved turbulence kinetic energy is near zero initially, and the modeled turbulence kinetic energy is typically much larger than it will be for the final LES/RANS solution. The choice of ensemble-averaging method may therefore be quite important for the modeled quantities due to a possible dependence on the initial conditions. The operator for advancing the ensemble-average of a general quantity Q is

$$\bar{Q}^{\,n} = \bar{Q}^{n-1}(1 - A) + AQ^n \tag{29}$$

with $A = \Delta t/\tau$. The time scale τ is defined as follows for three variants considered in this work.

Weighting no. 1,

$$\tau = t \tag{30a}$$

Weighting no. 2,

$$\tau = \min(t, t_{\mathrm{res}}) \quad (t < 4t_{\mathrm{res}}), \qquad \tau = t - 3t_{\mathrm{res}} \quad (t \geq 4t_{\mathrm{res}}) \tag{30b}$$

Weighting no. 3,

$$\tau = \min(t, t_{\mathrm{res}}) \tag{30c}$$

where $\tau_{\mathrm{res}} = L/u_\infty$ is defined in terms of the length of the domain L and the freestream velocity u_∞ weighting no. 3 is an exponentially

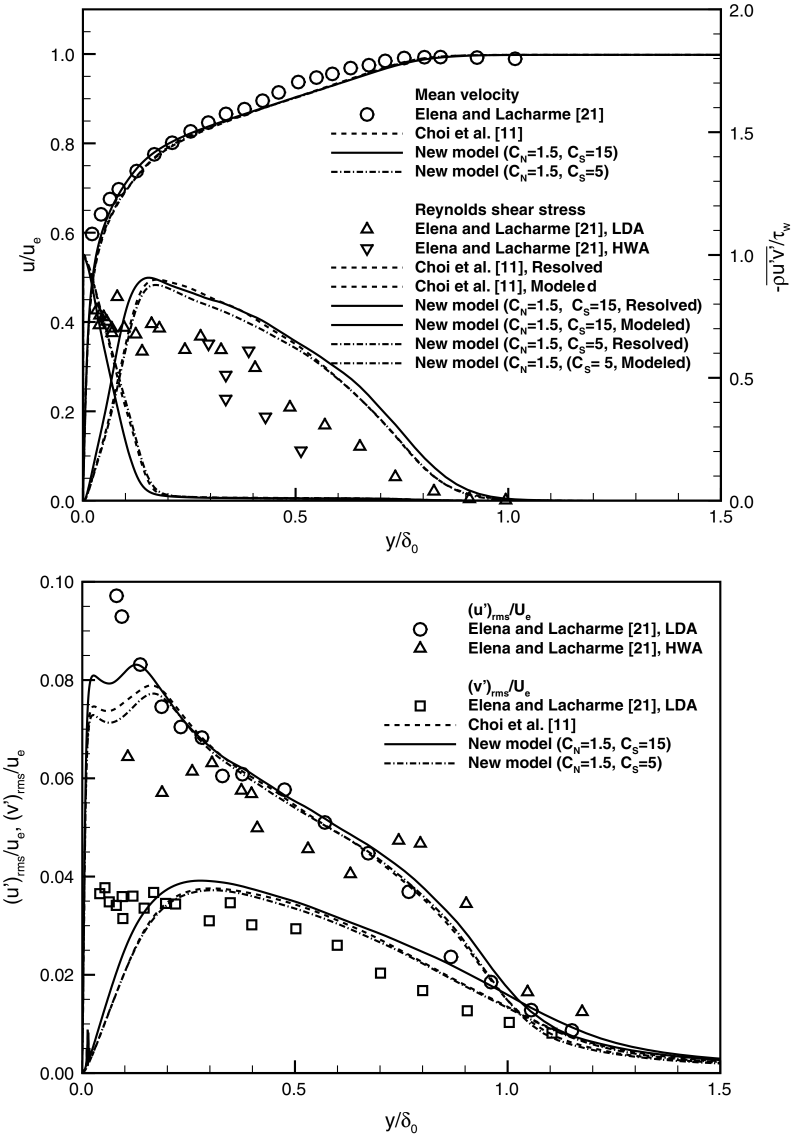

Fig. 3 Mean velocity and Reynolds shear stress (top) and rms axial velocity and rms normal velocity (bottom) versus normalized wall distance (Elena and Lacharme [21] experiment); HWA is hot-wire anemometry, and LDA is laser Doppler anemometry.

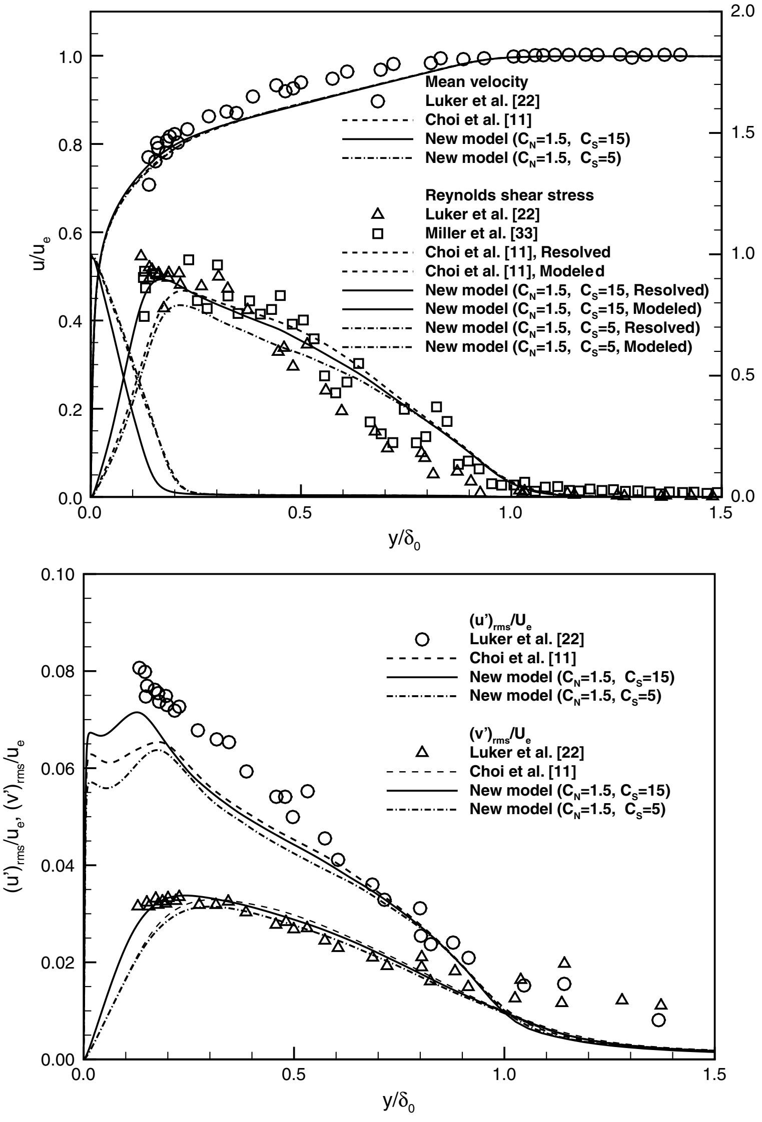

Fig. 4 Mean velocity and Reynolds shear stress (top) and rms axial velocity and rms normal velocity (bottom) versus normalized wall distance (Luker et al. [22] experiment).

weighted moving average, with the window set as one flow-through time, while weighting no. 1 is a conventional time average. Weighting no. 2 is a blend of a windowed average and a conventional one. The calibration of the LES/RANS model was performed using weighting no. 1 to determine the ensemble averages, and this method is used for all test cases discussed subsequently unless otherwise noted. The forms mentioned above may not be directly applicable to flows that do not yield a statistically steady state. More sophisticated averaging techniques, based on adaptive Kalman filtering, have been proposed to handle situations in which the mean flow itself may be unsteady over time scales much longer than those characteristic of turbulent motion [30]. While the use of ensemble-averaged quantities in a LES-type turbulence closure might not be ideal, the fact that ensemble-averaged data can contain important turbulence scale information has been leveraged in the development of improved subgrid models [31] and in other LES/RANS hybridization strategies [32].

Results

Flat-Plate Studies

Comparison with Experimental Data

Figures 3–5 compare predicted mean velocity, Reynolds shear stress, and rms normal and axial fluctuation intensities with experimental data for three compressible flat-plate boundary layers. The constant C_N is set to 1.5 for the new model, while the constant C_s is selected as 15 or as 5. Reynolds numbers based on the boundary-layer thickness are 5.59e4, 1.78e5, and 1.58e6 for the Elena and Lacharme [21], Luker et al. [22], and Smits and Muck [23] experiments, respectively. Other properties are listed in Table 1. The baseline meshes each contain 5.12 million cells and are designed so that 20 cells/boundary-layer thickness are present in the wall-transverse directions (X and Z). Significantly more resolution (greater than 100 cells/boundary-layer thickness) is present in the wall-normal direction. Mesh spacing parameters are presented in inner- and outer-layer coordinates in Table 2. Calculations performed using the original model with PPM [11] were repeated using the LD-PPM scheme to enable a consistent comparison. These results show several trends. First, the mean velocity is relatively unaffected by the model choice. The Reynolds shear-stress distributions, presented in terms of their modeled and resolved components, show that the decay in resolved Reynolds shear stress is compensated for by an increase in the modeled component. The 50% value in the normalized modeled Reynolds stress corresponds approximately to the 50% value in the time-averaged blending function. With the exception of the Smits and Muck [23] case (Fig. 5), the differences among Reynolds shear-stress profiles predicted by each model are small. Lowering the sharpening factor C_s from 15 to 5 leads to an increase in the modeled Reynolds shear-stress component, implying that the position of the time-averaged RANS-to-LES transition shifts further

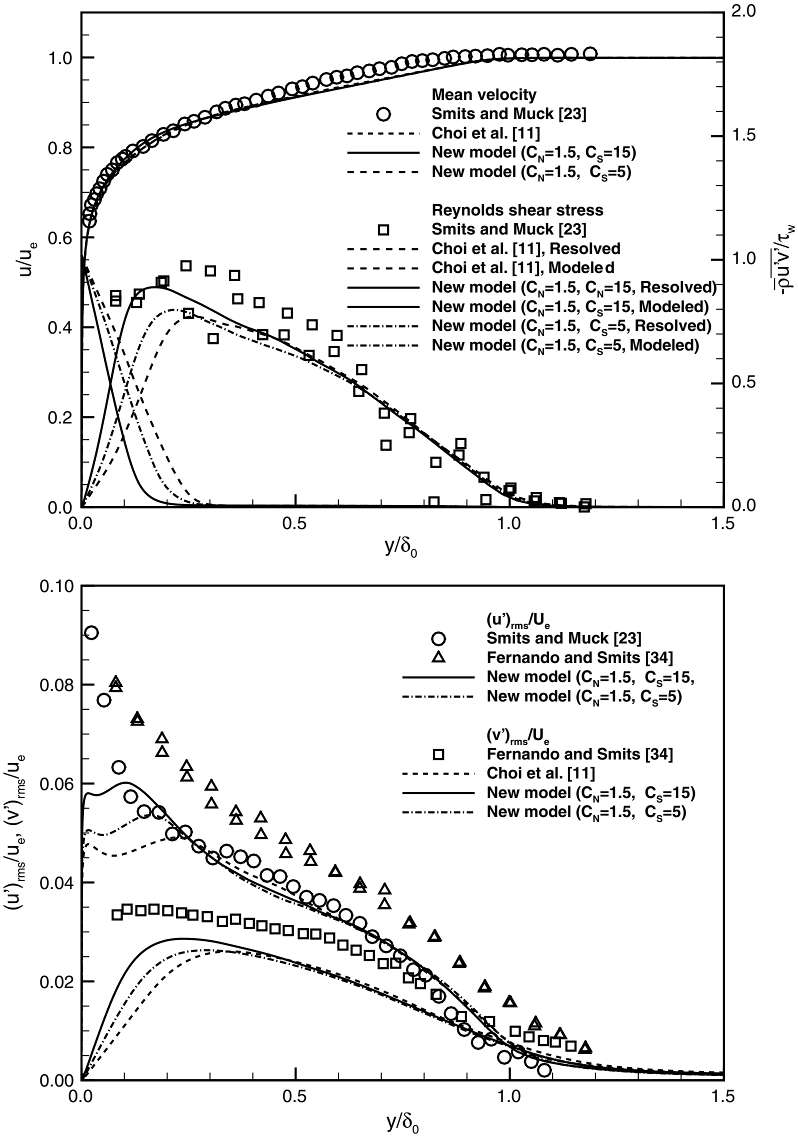

Fig. 5 Mean velocity and Reynolds shear stress (top) and rms axial velocity and rms normal velocity (bottom) versus normalized wall distance (Smits and Muck [23] experiment).

away from the wall. All models underpredict the peak in rms axial velocity indicated in all data sets at $y/\delta_0 < 0.2$. This appears to be a consequence of the damping effect of the RANS component of the model. It should be noted that the modeled contributions to the Reynolds normal stresses are not included in the rms velocity comparisons, as the Boussinesq approximation is known to be invalid for these components in the near-wall region. With the exception of the Smits and Muck [23] experiment, the model predictions for the rms normal velocity are in good agreement with experimental data. In all cases, the predictions provided by the new model are comparable with those of the original model.

Table 1 Freestream and boundary-layer properties for experiments considered in this study

Case	M_∞	δ_0, mm	U_∞, m/s	Re_δ	P_o, pa	T_o, K	C_f ($\times 10^{-3}$)
Elena and Lacharme [21]	2.32	10 (12)[a]	552	5.59×10^4	5.0×10^4	291	2.15
Luker et al. [22]	2.80	9.9	602	1.78×10^5	2.1×10^5	298	1.6
Smits and Muck [23]	2.79	25	562	1.58×10^6	6.9×10^6	263	1.07
Donovan et al. [15]	2.86	28	580	1.76×10^6	6.9×10^6	270	1.08

[a] Evaluated at 99.9% of boundary-layer edge velocity.

Table 2 Mesh spacing parameters for experiments considered in this study

Case	Δx, $\Delta z/\delta_0$	$\Delta y_{\max}/\delta_0$	$\Delta y_{\min}/\delta_0$	Δx^+, Δz^+	$\Delta y^+_{\max}$	$\Delta y^+_{\min}$
Elena and Lacharme [21]	0.05	0.026	0.0005	6.37	3.31	0.063
Luker et al. [22]	0.05	0.026	0.0005	13.21	6.87	0.132
Smits and Muck [23]	0.05	0.028	0.0002	85.78	48.03	0.343
Donovan et al. [15]	0.05	0.028	0.0002	85.78	48.03	0.343

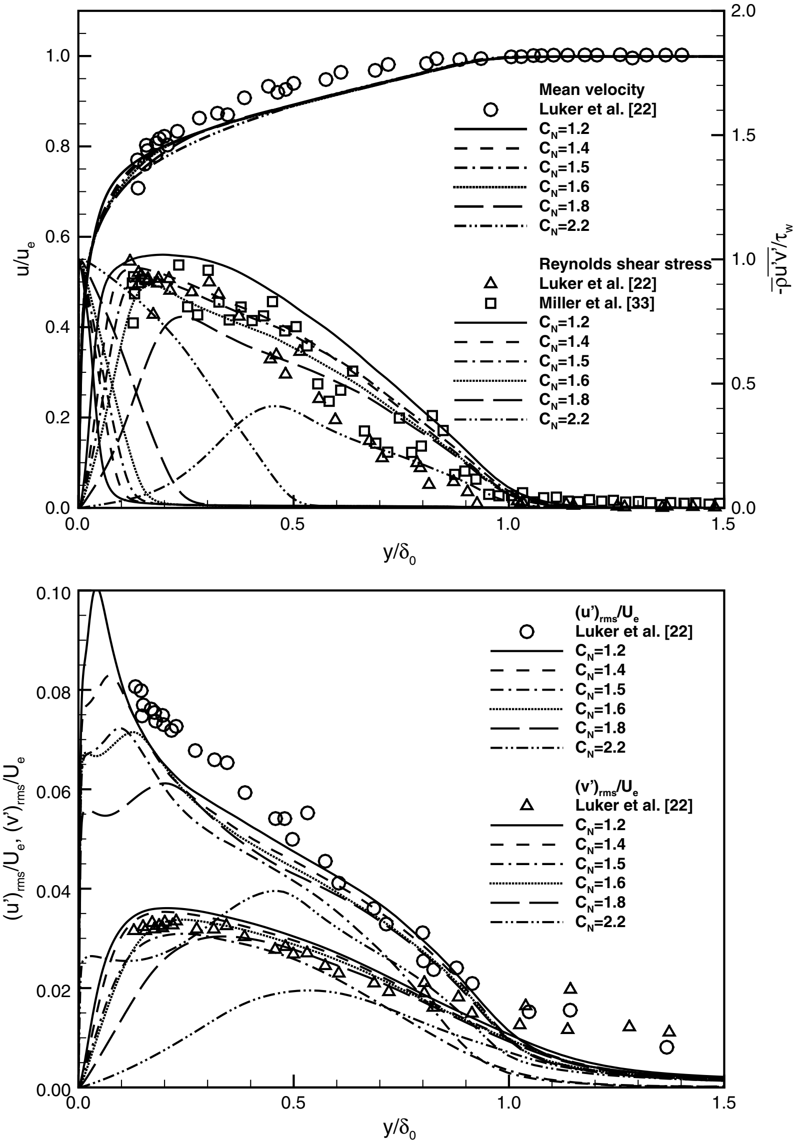

Fig. 6 Effect of C_N (Luker et al. [22] experiment).

Sensitivity to C_N

Figure 6 addresses the sensitivity of the predictions to variations in the model constant C_N. The experiment of Luker et al. [22] is considered in this evaluation. As expected, a trend of increasing the modeled Reynolds shear-stress component and decreasing the resolved component is evidenced with an increase in the model constant. As the model constant reduces, more of the resolved turbulence energy near the wall is captured, and the prediction of rms axial velocity, in particular, improves. This effect is accompanied, however, by an increase in the fullness of the velocity profile in the outer part of the logarithmic region ($0.1 < y/\delta_0 < 0.25$) and, as shown later, a decrease in the wall shear stress. The apparent overprediction of the resolved Reynolds shear stress for $C_N = 1.2$ is partly a result of this reduction in the wall shear stress. Even at the highest value of C_N considered (2.2), a significant amount of fluctuation energy is still contained in the outer layer. A shift to a RANS-like response would require even larger values of the model constant.

Sensitivity to Ensemble-Averaging Method

The sensitivity of the predictions to the method of ensemble-averaging is illustrated in Fig. 7 for the Luker et al. [22] and Smits and Muck [23] experiments. Comparisons with experimental data are again presented for the resolved Reynolds shear stress, but the velocity profiles are shown in inner-layer coordinates using the Van Driest I transformation. This transformation highlights the smoothness of the velocity profile in the inner region and indicates the degree to which a log-law mismatch [35] is observed. The sensitivity of the predictions to the method of ensemble-averaging is not high, but the conventional average (weighting no. 1) places the time-averaged RANS-to-LES transition somewhat further away from the wall. This implies that some of effects of the initial distribution of turbulence variables are maintained when conventional averaging is used. Weighting nos. 2 and 3 provide very similar solutions for both cases. A severe log-law mismatch is not observed in any case, but the velocity profile is not completely smooth, exhibiting a small hump that is reduced in size as the time-averaged transition position shifts further away from the wall. In all cases, the computed profiles in the logarithmic and wake regions lie above the theoretical solution. This is a consequence of a slight underprediction of the wall shear stress exhibited by all models tested.

Sensitivity to Mesh Refinement

The sensitivity of the model predictions to mesh refinement in the wall-transverse directions (X and Z) is illustrated in Fig. 8 for the Elena and Lacharme [21] and Smits and Muck [23] experiments. The model constants C_N and C_s are set to 1.5 and 15, respectively, and weighting no. 2 is used. For the coarse meshes, the mesh spacing in the X and Z directions is increased by a factor of 2 (10 cells per boundary-layer thickness). The fine meshes decrease the mesh

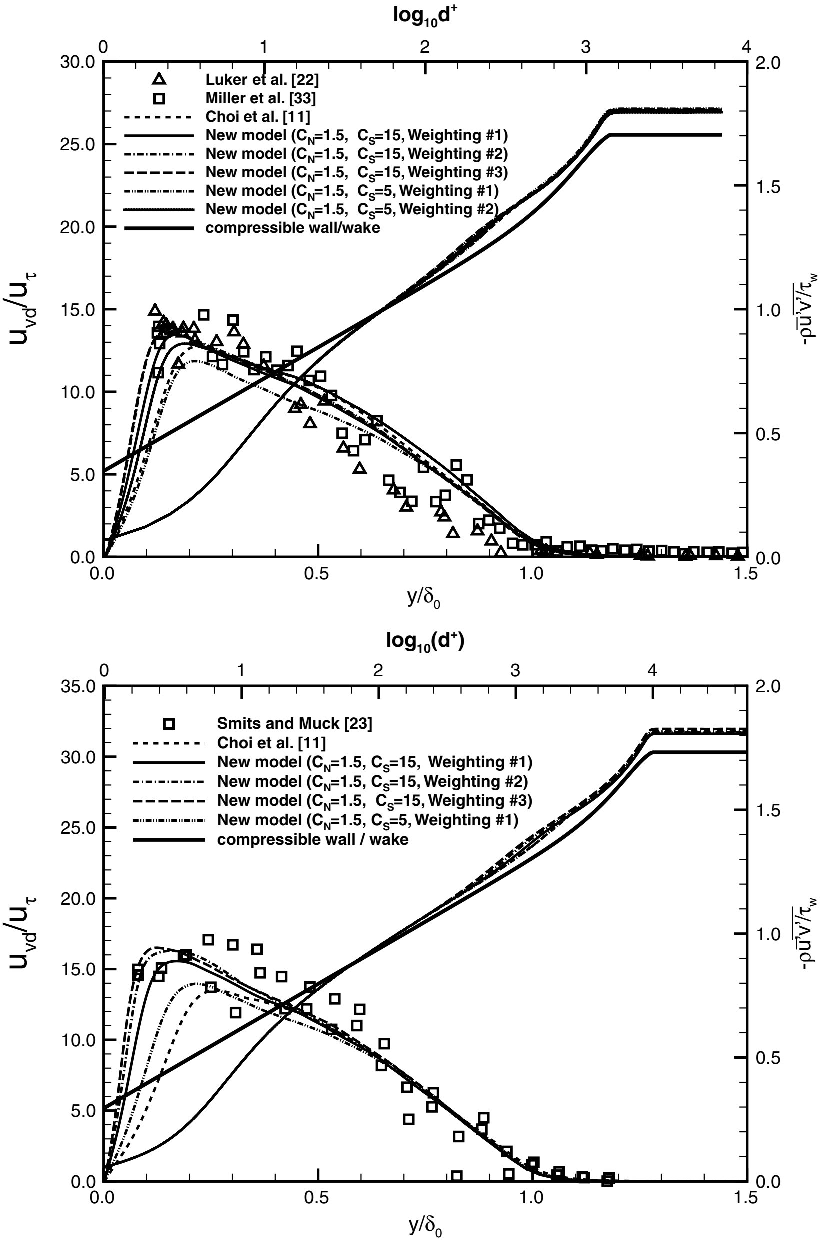

Fig. 7 Effect of ensemble-averaging technique (top: Luker et al. [22], bottom: Smits and Muck [23]).

spacing in the X and Z directions by a factor of 2/3 (30 cells per boundary-layer thickness). Mean axial velocity and resolved and modeled Reynolds shear stress are plotted in the figures. The predictions for the Elena and Lacharme [21] experiment (the lowest-Reynolds-number case) are the most sensitive to mesh refinement, with the finer-mesh solution displaying a more linear decay in the resolved Reynolds shear stress in the outer part of the boundary layer. The effective RANS-to-LES transition location also shifts toward the wall for the finer mesh. It should be noted that the maximum eddy viscosity levels for the Elena and Lacharme case are of the order of 10 to 20 times the molecular viscosity; the RANS component has a comparatively minor influence on the structure of the flow, particularly as the mesh is refined. The solutions for the Smits and Muck [23] boundary layer show less sensitivity to mesh refinement, though the general trends are the same as observed for the Elena and Lacharme [21] experiment.

Comparison with IDDES

An alternative wall-modeled LES strategy (termed IDDES) has been developed by Shur et al. [4] as an extension of the DDES model [3]. The general idea adopted by IDDES is that the mesh spacing, plus the presence of initial fluctuation content, will dictate whether the model responds as a wall-modeled LES, as DDES, or as a pure RANS model. It is thus a more general framework than our model, which is strictly a type of wall-modeled LES. The wall-modeled LES branch of IDDES differs from ours in several respects. First, the Menter shear stress transport model is used as the basis, rather than the Menter BSL model. Secondly, only the destruction term in the turbulence kinetic energy equation is modified through the action of a blending function. The eddy viscosity responds to the combined influences of the turbulence kinetic energy, the turbulence frequency, and a specified filter width; there is no separate definition of a subgrid eddy viscosity. In our model, the eddy viscosity description is designed to shift between RANS and LES branches, and in principle, different subgrid and RANS models could be employed. The blending functions used in IDDES are fundamentally based on the ratio of the wall distance to a filter width, and thus the transition between RANS and LES branches occurs at fixed locations for a particular grid. In our model, the instantaneous transition location will migrate in response to the resolved and ensemble-averaged solution. The IDDES method uses flow-dependent enhancement functions to augment the RANS component in the vicinity of the transition location; the authors argue that such functions are crucial

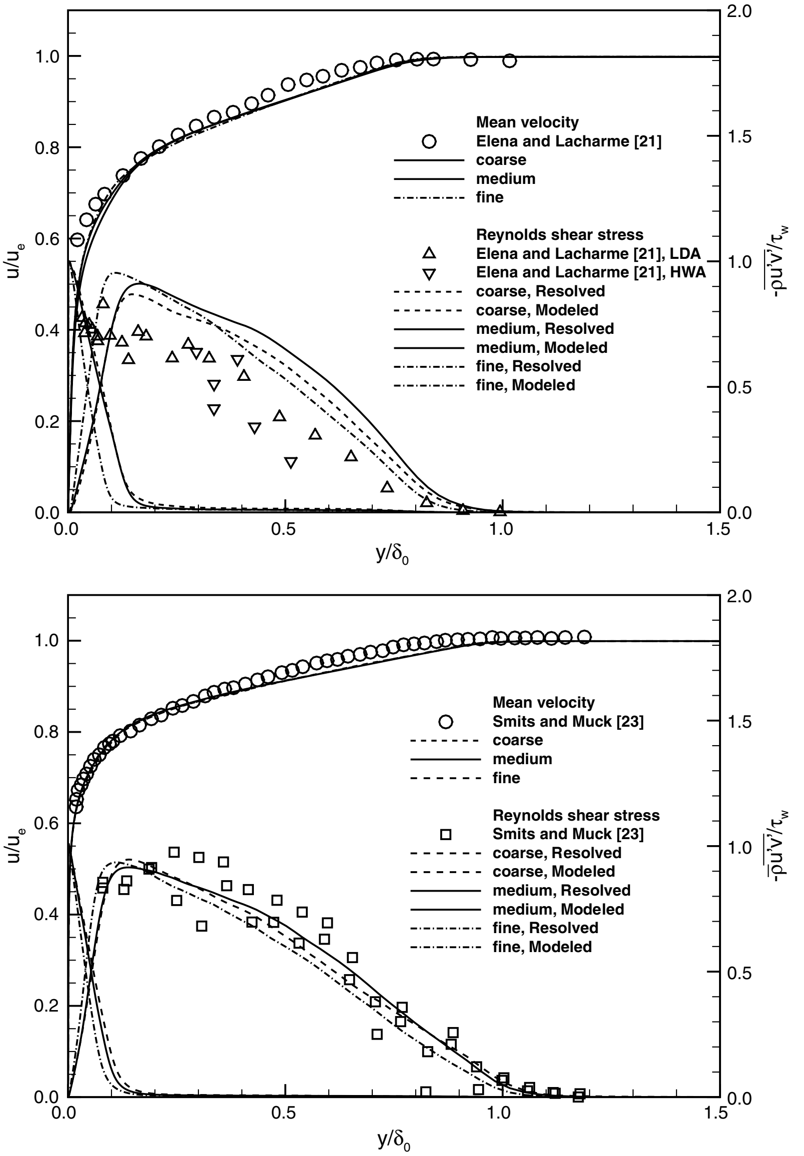

Fig. 8 Effect of mesh refinement in wall-transverse directions (top: Elena and Lacharme [21], bottom: Smits and Muck [23]).

for combating log-law mismatch. For the array of flat-plate boundary layers considered in this work, the transition location as calculated in the IDDES model is at $y/\delta_0 = 1/40$. In wall coordinates, this places the transition at $d^+ = 17.8$, 36.7, and 251.8 for the Elena and Lacharme [21], Luker et al. [22], and Smits and Muck [23] cases, respectively The first two locations are near the beginning of the logarithmic region, while the latter is more toward the middle of the region.

Figures 9 and 10 compare solutions obtained using the new model ($C_N = 1.5$, $C_s = 15$) with those from IDDES and with Menter BSL RANS solutions for the Elena and Lacharme [21] and Smits and Muck [23] cases. The RANS velocity solutions agree very well with the compressible law of the wall and with the experimental data and thus might be used as a reference to assess the predictive capability of the other models. The resolved turbulence kinetic energy and Reynolds shear stress are plotted for the LES/RANS models, while the modeled turbulence kinetic energy and Reynolds shear stress are plotted for the RANS model. The axial velocity is plotted versus $\log_{10}(y/\delta_0)$ and is scaled by the freestream velocity instead of the friction velocity. This removes ambiguities associated with the possible underprediction of the wall shear stress. Both LES/RANS models predict outer-layer values of turbulence kinetic energy and Reynolds shear stress that are comparable with those modeled using RANS. The model responses differ greatly in the inner layer, with the IDDES solution exhibiting a peak in turbulence kinetic energy also captured in the $C_N = 1.2$ solution of Fig. 6. The rapid diminishing of the resolved fluctuation energy near the wall by the new model is again in evidence. The new LES/RANS model (with $C_N = 1.5$) yields velocity profiles that are in close accord with the RANS solutions, whereas the IDDES solutions show an increase in velocity toward the outer part of the logarithmic region followed by a decrease in velocity in the inner part of the layer. Figure 11 presents a scatter plot of predicted skin friction versus C_N for all of the models considered in this study. Groups of data corresponding to each case are encircled by polygons. For IDDES, C_N is arbitrarily set to one, while for Choi et al. [11] C_N is arbitrarily set to 1.5. The general trend is that all of the LES/RANS models underpredict the wall shear-stress level, with the IDDES and $C_N = 1.2$ solutions showing the largest deviations. As indicated in Table 1, the RANS skin-friction predictions are very close to the experimental values. Based on these results and the others presented, it appears that a RANS-to-LES transition that occurs near the inner edge of the logarithmic layer can result in insufficient dissipation of resolved turbulence energy in the outer part of the logarithmic layer. Axial fluctuation-intensity predictions improve, but inaccuracies in the wall shear stress and inner-layer velocity profile appear. Shifting the RANS-to-LES transition toward the middle and outer parts of the logarithmic layer, as is done in the new model with $C_N = 1.5$–1.6, yields closer agreement with theory and with RANS predictions for the velocity profile but leads to an underprediction of the resolved axial fluctuation intensity in the near-wall region.

16 Degree Smooth Compression Corner

The LES/RANS models described in this paper are also applied to a Mach 2.86, 16 deg smooth-compression-corner interaction mapped by Donovan et al. [15,16]. The flow conditions are shown in Table 1. The specific variants tested are the original model of [6] (with the model constant $\alpha_1 = 13.06s + 76.7$ fitted as a function of the surface coordinate s), the new model with $C_N = 1.5$ and $C_s = 15$ using weighting no. 1 for ensemble-averaging, and the new model with $C_N = 1.5$ and $C_s = 15$ using weighting no. 2 for ensemble-averaging. The mesh extends from $X = -0.28$ to 0.2717 m in the streamwise direction, with $X = 0$ m corresponding to the start of the 16 deg turn. The mesh extends 0.14 m in the wall-normal (Y) direction and ±0.0756 m in the spanwise (Z) direction. The mesh resolution is such that 20 cells/incoming boundary-layer thickness are present in the wall-transverse directions, and the total number of interior mesh cells is 8.64 million. The recycle plane is located 7.5 boundary-layer thicknesses ($\delta = 2.5$ cm) downstream of the inflow plane.

An isosurface of swirl strength (7500 s^{-1}), colored by temperature, is shown in Fig. 12 for the Donovan et al. [15] experiment. The swirl strength is defined as the imaginary portion of the complex eigenvalue of the local velocity gradient tensor. The higher the value of the swirl strength, the shorter the time required for a fluid particle to swirl about a vortex core. Higher values of the swirl strength typically correspond to smaller-scale turbulent structures, and the distribution of the swirl strength can provide an approximate measure of the distribution of the sizes of turbulent eddies. The value chosen (7500 s^{-1}) is large enough to highlight the presence of longitudinally oriented vortical structures in the recovering boundary layer downstream of the isotropic compression. These appear to arise from amplification of inhomogeneities in the incoming boundary layer and have been observed in both experiments and computations of compression-ramp flows [6,36].

Predictions for mean-flow properties for the Donovan et al. [15] experiment are shown in Figs. 13–16. Time- and span-averaging of the instantaneous data is used to generate the mean values. Surface pressure distributions in Fig. 13 show evidence of a smooth compression process unaffected by local flow separation. Figure 14 shows that, relative to the original model, the new LES/RANS model yields better agreement with surface skin-friction measurements of Donovan [16] within and downstream of the compression region.

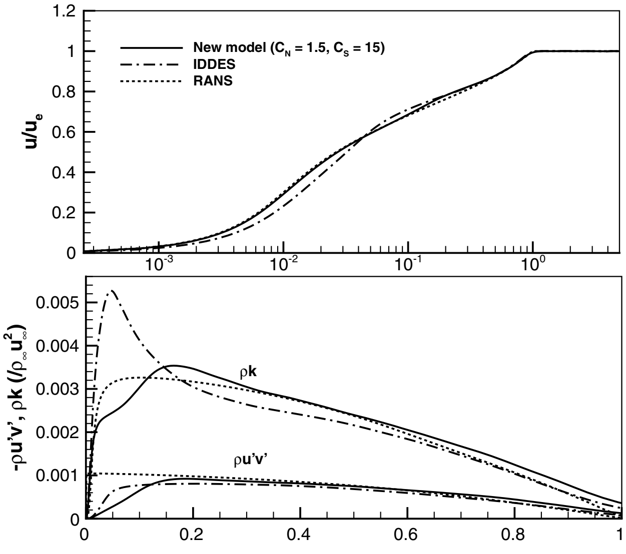

Fig. 9 Reynolds shear stress, turbulence kinetic energy, and mean velocity predictions for different turbulence models (Elena and Lacharme [21] experiment).

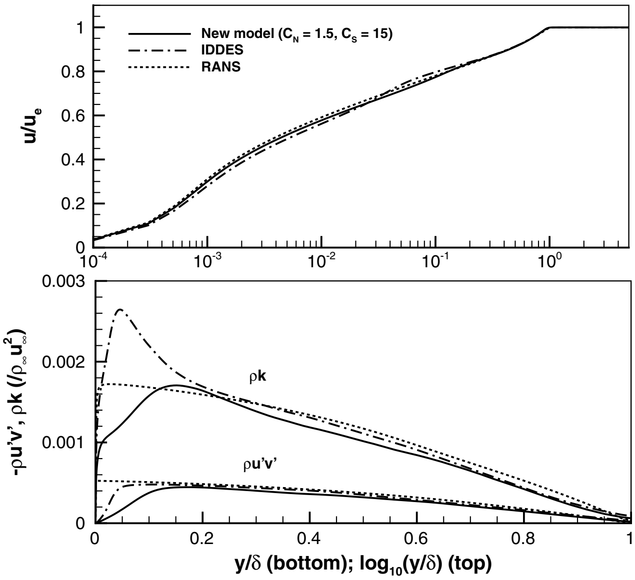

Fig. 10 Reynolds shear stress, turbulence kinetic energy, and mean velocity predictions for different turbulence models (Smits and Muck [23] experiment).

Predictions of integral boundary-layer properties (Fig. 15) for all models are in good agreement with experimental results upstream and downstream of the compression region. The lack of good agreement within the interaction region itself may be a consequence

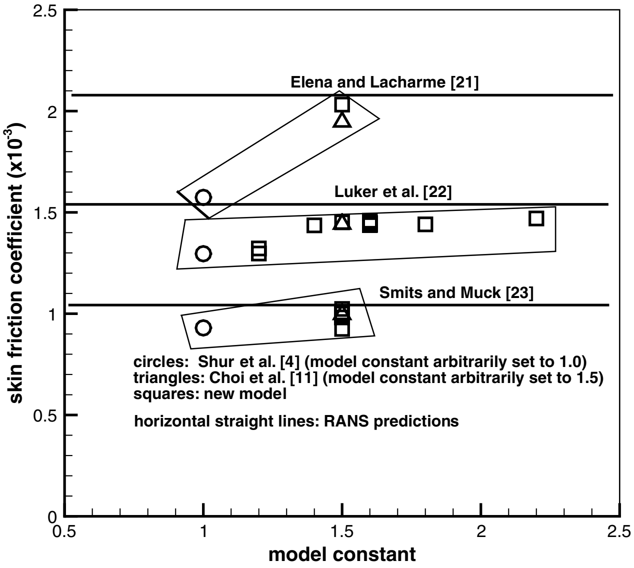

Fig. 11 Skin friction vs model constant.

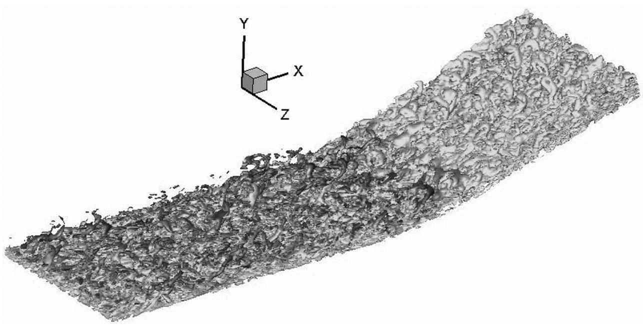

Fig. 12 Isosurfaces of swirl strength (7500 s^{-1}) colored by temperature values (Donovan et al. [15] experiment).

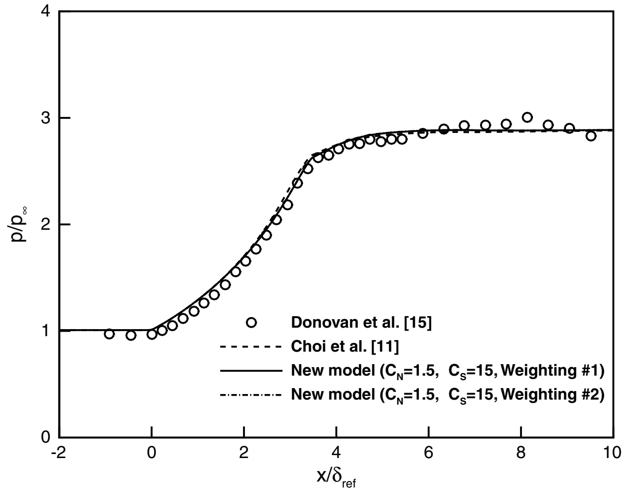

Fig. 13 Surface wall pressure distributions (Donovan et al. [15] experiment).

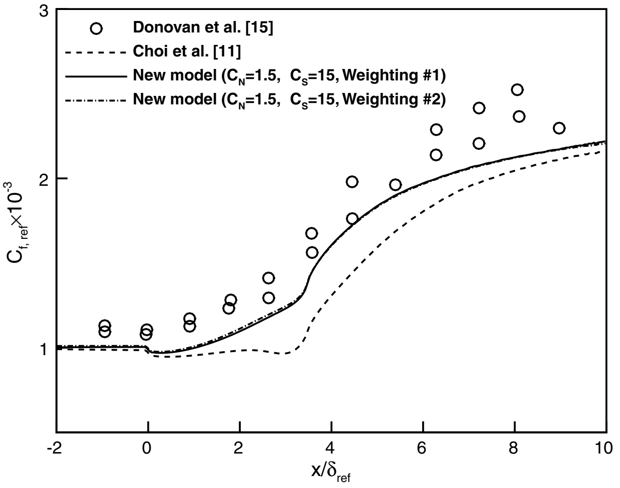

Fig. 14 Surface skin-friction distributions (Donovan et al. [15] experiment).

of ambiguities in the definition of the boundary-layer edge in both the computational and experimental results.

Figure 16 compares mean mass-flux distributions (based on the velocity component tangential to the surface) with experimental hot-wire data throughout the interaction. Good agreement is indicated in

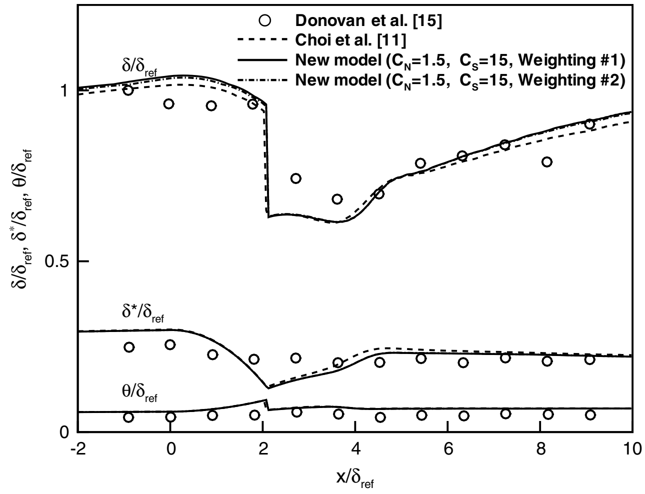

Fig. 15 Boundary-layer properties (Donovan et al. [15] experiment).

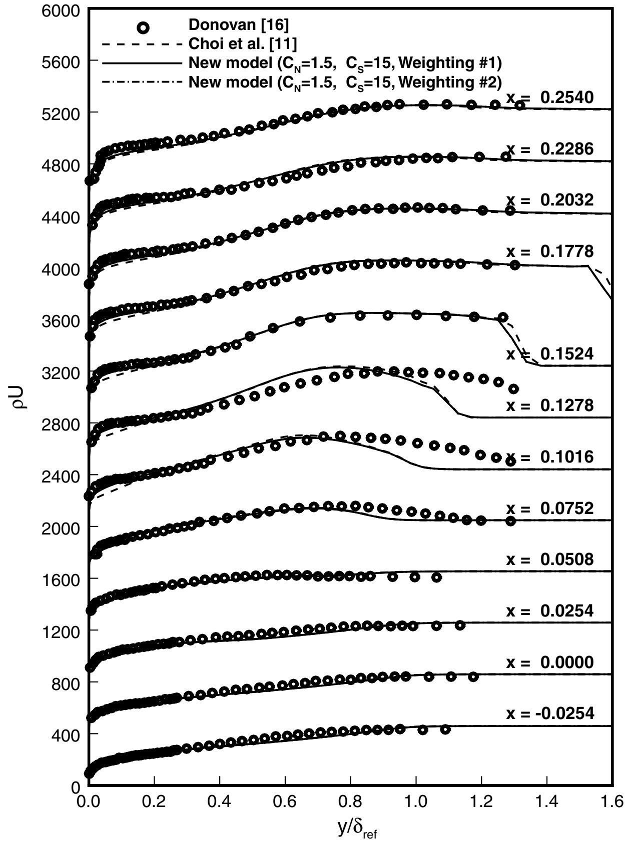

Fig. 16 Streamwise mass-flux distributions throughout the interaction region (Donovan et al. [15] experiment).

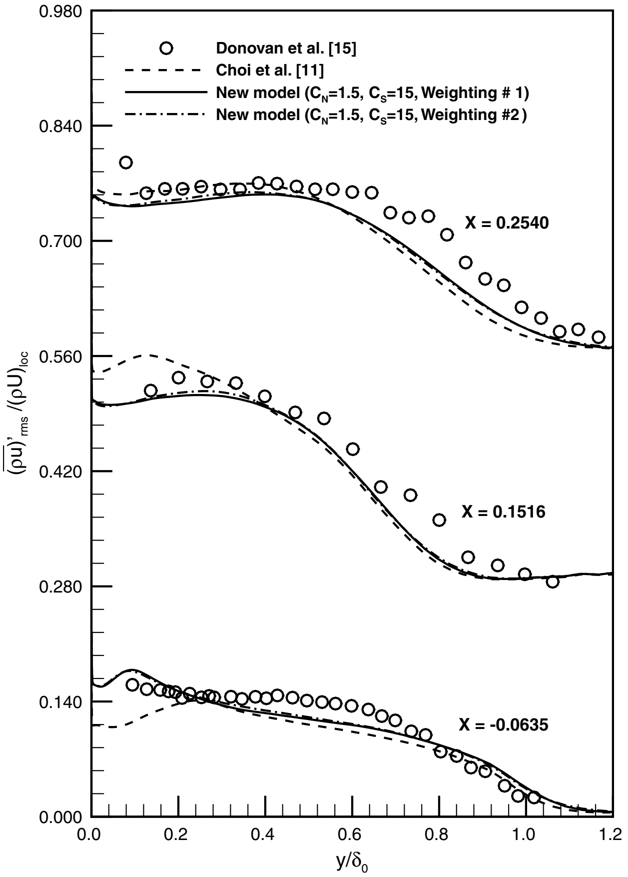

Fig. 17 Mass-flux fluctuation intensity profiles at different streamwise stations (Donovan et al. [15] experiment).

general, though the computed profiles do show an underprediction of the mass-flux distributions in the near-wall region downstream of the compression region. Locations in the flowfield associated with the coalescence of compression waves into a shock wave (Fig. 16, $X = 0.1016$ and 0.1278 stations) are also not well predicted. The hot-wire measurements may not be as accurate in this region. The new model predicts a faster recovery of the inner part of the boundary layer downstream of the compression region and provides slightly better agreement with experiment in this region.

Figure 17 compares mass-flux fluctuation intensity predictions with experimental data at three streamwise locations within the interaction region. The mass-flux fluctuation intensity is computed according to

$$(\overline{[(\rho\tilde{u}_1)']^2})^{1/2} = [\overline{(\rho\tilde{u}_1)^2} - \overline{\rho\tilde{u}_1}\,\overline{\rho\tilde{u}_1}]^{1/2} \tag{31}$$

where the overbar represents time- and span-averaging of the grid-filtered data and $\tilde{u}_j$ is the velocity vector expressed in a coordinate system that is aligned with the compression-corner surface. At its peak in the incoming boundary layer, the maximum value of the mass-flux fluctuation intensity is about 15%, increasing to a maximum of about 25% midway along the compression-ramp portion. As the boundary layer begins to relax back to a new equilibrium state, the mass-flux fluctuation intensity diminishes. The LES/RANS predictions are in good agreement with experimental data at every station, with the new model providing better overall agreement nearer to the surface.

Favre-averaged Reynolds stresses are computed according to

$$\bar{\rho}\,\overline{\tilde{u}_i''\tilde{u}_j''} = \overline{\rho\tilde{u}_i\tilde{u}_j} - \frac{\overline{\rho\tilde{u}_i}\,\overline{\rho\tilde{u}_j}}{\bar{\rho}} \tag{32}$$

Only the resolved Reynolds stresses are captured in this approach, but as the experimental data does not extend far into the wall layer, this is adequate for comparison. Figure 18 compares experimental measurements of the Reynolds axial stress with computational predictions. Good agreement is generally indicated, though calculations performed using the original LES/RANS model do overpredict the peak value of the Reynolds axial stress at the $X = 0.1516$ m data station, which is near the point where the isentropic compression ends. The new model provides improved results at this station. Evidence obtained from earlier shock impingement and compression-ramp studies [6,12] indicates that the original model may overamplify turbulent fluctuations in the near-wall region downstream of a strong compression. This problem may be related to a collapse in the blending function toward the wall, which enables larger turbulent eddies to interact with the wall without significant attenuation. The fact that the new model improves upon this response is encouraging.

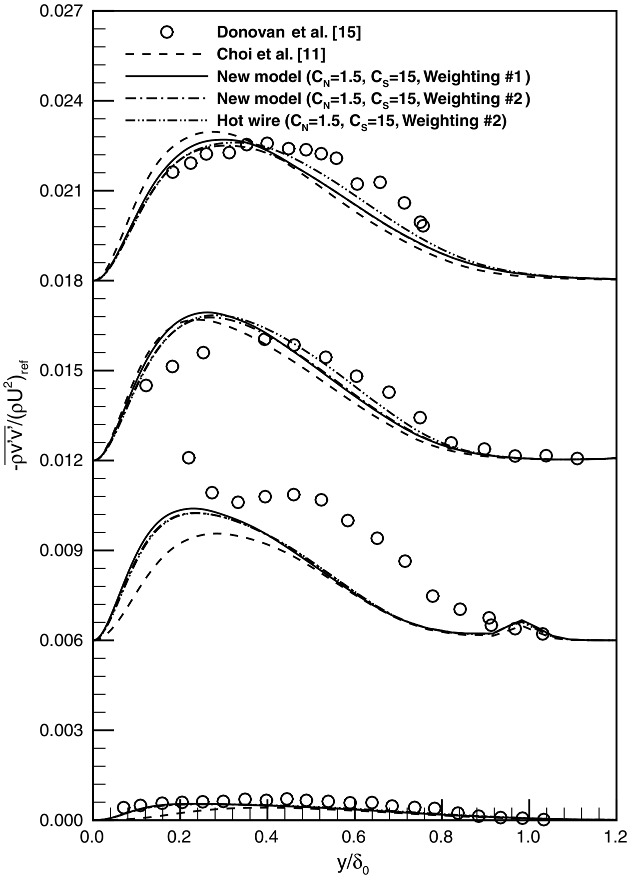

Fig. 19 Reynolds normal stress profiles at different streamwise stations (Donovan et al. [15] experiment).

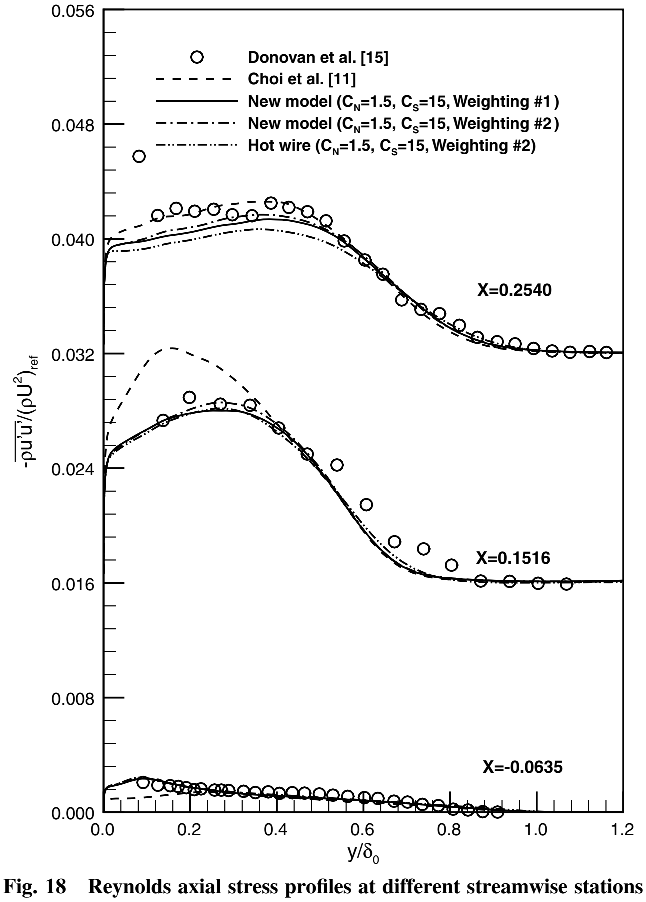

Fig. 18 Reynolds axial stress profiles at different streamwise stations (Donovan et al. [15] experiment).

Comparisons with the measured Reynolds normal stress (Fig. 19) show that the trends regarding amplification of this component are in agreement with those shown in the experimental data and are consistent with those evidenced in Figs. 17 and 18. Agreement with experiment is poor for the Reynolds shear stress (Fig. 20), as the computations overpredict the measured values by more than a factor of 2 at the most downstream stations. The experimental data show a marked decrease in the amplification rate of the Reynolds shear stress downstream of the end of the compression region. The calculations do not show this response, and neither the experimental data nor the computational predictions for the other Reynolds stress components show such a rapid return to equilibrium.

To examine whether the procedures used for extracting the Reynolds stress values could be at fault, we also consider extracting statistics that are equivalent to those obtained using hot-wire anemometry. The normal wire provides mass-flux fluctuations $(\rho\tilde{u}_1)'$, with the subscript 1 indicating the direction tangent to the compression-corner surface. The combination of normal and crossed

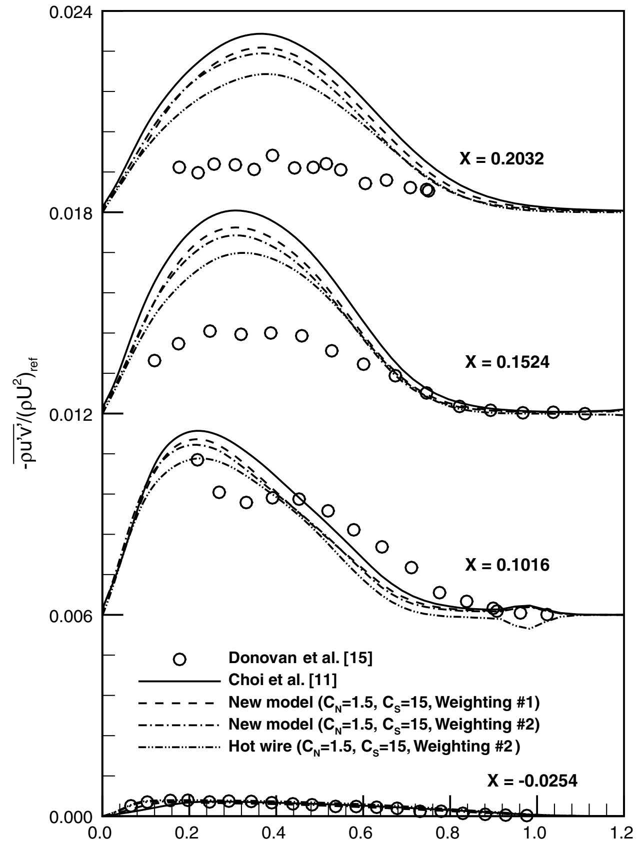

Fig. 20 Reynolds shear-stress profiles at different streamwise stations (Donovan et al. [15] experiment).

or inclined wires provides the mass-flux fluctuation and an estimate of fluctuations in the angle between the probe axis and the freestream flow [16]. These can be combined to yield an estimate of the velocity fluctuation in the direction normal to the surface. The strong Reynolds analogy [17] is used to convert fluctuations in the mass flux to fluctuations in the tangential velocity component. Thus, we have

$$\bar{\rho}\,\overline{\tilde{u}_1''\tilde{u}_2''} = (\overline{\rho\tilde{u}_1\tilde{u}_2} - \overline{\rho\tilde{u}_1}\,\overline{\tilde{u}_2})/(1+(\gamma-1)\overline{\tilde{M}_1^2}) \tag{33}$$

$$\bar{\rho}\,\overline{\tilde{u}_1''\tilde{u}_1''} = [\overline{(\rho\tilde{u}_1)^2} - \overline{\rho\tilde{u}_1}\,\overline{\rho\tilde{u}_1}]/[\bar{\rho}(1+(\gamma-1)\overline{\tilde{M}_1^2})^2] \tag{34}$$

$$\bar{\rho}\,\overline{\tilde{u}_2''\tilde{u}_2''} = \bar{\rho}[\overline{(\tilde{u}_2)^2} - \overline{\tilde{u}_2}\,\overline{\tilde{u}_2}] \tag{35}$$

where the Mach number $\overline{\tilde{M}_1^2}$ is based on the average tangential velocity component. Reynolds stress calculations using this procedure are also shown in Figs. 18–20. The Reynolds normal- and shear-stress profiles extracted in this fashion are generally lower in magnitude than those extracted using Eq. (32). The differences are slight, meaning that the extraction procedure is not the cause of the discrepancies described above. In all comparisons, only a slight effect of the choice of the weighting method used in ensemble-averaging of some of the model components can be seen.

Conclusions

A new LES/RANS model has been presented in this work. The new model is designed to transition from unsteady RANS to LES as the boundary layer shifts from its logarithmic behavior to its wakelike response. In contrast to previous developments of this idea [6,11], facilitating this transition does not require a problem-specific calibration of a model constant. Instead, the resolved turbulence kinetic energy, ensemble-averaged modeled turbulence kinetic energy and turbulence frequency, and time-resolved turbulence frequency are used to form an estimate of an outer-layer length scale that is nearly Reynolds-number-independent. The ratio of this outer-layer length scale with an inner scale (proportional to the wall distance) is used to construct a blending function that requires the specification of two model constants, one (C_N) that directly scales the argument of the blending function and another (C_s) that controls the sharpness of the function. Calculations of flat-plate boundary layers over a wide range of Reynolds numbers show that the new model provides results for mean and second-moment statistics that are in good agreement with experiment and are comparable with those obtained using the original model. Values of C_N between 1.5 and 1.6 provide good predictions. The results are not especially sensitive to the manner in which ensemble-averaging of the turbulence quantities is performed or to mesh refinement in the wall-transverse directions. Comparisons with results from the IDDES model [4] indicate that IDDES performs similarly to the new model when C_N is chosen small enough (1.2) to force a transition from RANS to LES in the inner part of the logarithmic region. Though no log-law mismatch is observed, the velocity predictions for both IDDES and the new model with $C_N = 1.2$ deviate from the expected behavior in the outer part of the logarithmic region. The wall shear stress is also reduced, relative to RANS predictions and experimental data, but predictions of the axial fluctuation intensity near the wall improve.

Calculations of Mach 2.86 flow over a 16 deg smooth compression corner have also been performed. Comparisons with surface- and boundary-layer integral properties show good agreement with experiment for all model variations, though the new model provides better predictions of the skin-friction level downstream of the compression region. Comparisons with Reynolds stress profiles extracted from hot-wire measurements show good agreement with experiment for mass-flux fluctuation intensity, Reynolds axial stress, and Reynolds normal stress, but poor agreement for the Reynolds shear stress in the recovery region downstream of the compression zone. Modifying the computational data-extraction procedure to mimic more closely the techniques used in the experiment does not significantly improve agreement with experiment for the Reynolds shear stress.

Acknowledgments

The work of D. Gieseking and J. Edwards is supported by the U.S. Army Research Office (W911NF-08-1-0430, monitored by Frederick Ferguson). The work of J.-I. Choi is supported by NASA under Cooperative Agreement NNX07AC27A-S01 and by the WCU (World Class University) program through the National Research Foundation of Korea funded by the Ministry of Education, Science and Technology (R31-2008-000-10049-0). The work of H. A. Hassan is supported by the National Center for Hypersonic Combined-Cycle Propulsion. Computer resources have been provided by the High Performance Computing component of North Carolina State University's Information Technologies Division and by the U.S. Department of Defense's High Performance Computing system. We gratefully acknowledge Alexander Smits for providing J. Donovan's thesis to us.

References

[1] Knight, D., and Degrez, G., "Shock Wave/Boundary Layer Interactions in High Mach Number Flows—A Critical Survey of Current CFD Prediction Capabilities," AGARD AR-319, Vol. 2, 1997.

[2] Spalart, P. R., Jou, W.-H., Strelets, M., and Allmaras, S. R., "Comments on the Feasibility of LES for Wings and on a Hybrid RANS/LES Approach," *1st AFOSR Conference on DNS/LES*, Aug. 1997.

[3] Spalart, P. R., Deck, S., Shur, M. L., Squires, K. D., Strelets, M., and Travin, A., "A New Version of Detached-Eddy Simulation, Resistant to Ambiguous Grid Densities," *Theoretical and Computational Fluid Dynamics*, Vol. 20, 2006, pp. 181–195. doi:10.1007/s00162-006-0015-0

[4] Shur, M. L., Spalart, P. R., Strelets, M. K., and Travin, A. K., "A Hybrid RANS-LES Approach with Delayed DES and Wall-Modeled LES Capabilities," *International Journal of Heat and Fluid Flow*, Vol. 29,

No. 6, 2008, pp. 1638–1649.
doi:10.1016/j.ijheatfluidflow.2008.07.001

[5] Temmerman, L., Hadziabdic, M., Leschziner, M. A., and Hanjalic, K., "A Hybrid Two-Layer URANS-LES Approach for Large Eddy Simulation at High Reynolds Numbers," *International Journal of Heat and Fluid Flow*, Vol. 26, 2005, pp. 173–190.
doi:10.1016/j.ijheatfluidflow.2004.07.006

[6] Edwards, J. R., Choi, J-I., and Boles, J. A., "Hybrid Large-Eddy/Reynolds-Averaged Navier–Stokes Simulation of a Mach-5 Compression Corner Interaction," *AIAA Journal*, Vol. 46, No. 4, 2008, pp. 977–991.
doi:10.2514/1.32240

[7] Hadjadj, A., and Dussauge, J. P., "Shock Wave Boundary Layer Interaction," *Shock Waves*, Vol. 19, No. 6, 2009, pp. 449–452.
doi:10.1007/s00193-009-0238-2

[8] Garnier, E., "Stimulated Detached Eddy Simulation of Three-Dimensional Shock/Boundary Layer Interaction," *Shock Waves*, Vol. 19, 2009, pp. 479–486.
doi:10.1007/s00193-009-0233-7

[9] Peterson, D. M., Subbareddy, P. K., and Candler, G. V., "Detached Eddy Simulations of Flush Wall Injection into a Supersonic Freestream," AIAA Paper 2006-4576, 2006.

[10] Peterson, D., and Candler, G., "Supersonic Combustion Fuel-Injector Simulations Using a Hybrid RANS/LES Approach," AIAA Paper 2010-411, 2010.

[11] Choi, J.-I., Edwards, J. R., and Baurle, R. A., "Compressible Boundary Layer Predictions at High Reynolds Number Using LES/RANS Models," *AIAA Journal*, Vol. 47, No. 9, 2009, pp. 2179–2193.
doi:10.2514/1.41598

[12] Ghosh, S., Choi, J.-I., and Edwards, J. R., "Simulation of Shock/Boundary-Layer Interactions with Bleed Using Immersed-Boundary Methods," *Journal of Propulsion and Power*, Vol. 26, No. 2, 2010, pp. 203–214.
doi:10.2514/1.45297

[13] Boles, J. A., Edwards, J. R., and Choi, J.-I., "Large-Eddy/Reynolds-Averaged Navier–Stokes Simulations of Sonic Injection into Mach 2 Crossflow," *AIAA Journal*, Vol. 48, No. 7, 2010, pp. 1444–1456.
doi:10.2514/1.J050066

[14] Jayaram, M., Taylor, M. W., and Smits, A. J., "The Response of a Compressible Turbulent Boundary Layer to Short Regions of Concave Surface Curvature," *Journal of Fluid Mechanics*, Vol. 175, 1987, pp. 343–362.
doi:10.1017/S0022112087000429

[15] Donovan, J. F., Spina, E. F., and Smits, A. J., "The Structure of a Supersonic Turbulent Boundary Layer Subjected to Concave Surface Curvature," *Journal of Fluid Mechanics*, Vol. 259, 1994, pp. 1–24.
doi:10.1017/S0022112094000017

[16] Donovan, J. F., "The Structure of Supersonic Turbulent Boundary Layers Subjected to Concave Surface Curvature," Ph.D. Dissertation, Princeton Univ., Princeton, NJ, 1989.

[17] Smits, A. J., and Dussauge, J.-P., *Turbulent Shear Layers in Supersonic Flow*, 2nd ed., Springer, New York, 2006.

[18] Menter, F. R., "Two-Equation Eddy-Viscosity Turbulence Models for Engineering Applications," *AIAA Journal*, Vol. 32, No. 8, August 1994, pp. 1598–1605.
doi:10.2514/3.12149

[19] Lenormand, E., Sagaut, P., Ta Phuoc, L., and Comte, P., "Subgrid-Scale Models for Large-Eddy Simulations of Compressible, Wall-Bounded Flows," *AIAA Journal*, Vol. 38, 2000, pp. 1340–1350.
doi:10.2514/2.1133

[20] Fan, T. C., Edwards, J. R., Hassan, H. A., and Baurle, R. A., "Hybrid Large-Eddy/Reynolds-Averaged Navier–Stokes Simulations of Shock-Separated Flows," *Journal of Spacecraft and Rockets*, Vol. 41, No. 6, 2004, pp. 897–906.
doi:10.2514/1.3735

[21] Elena, M., and Lacharme, J. P., "Experimental Study of a Supersonic Turbulent Boundary Layer Using a Laser Doppler Anemometer," *Journal de Mecanique Theorique et Appliquee*, Vol. 7, No. 2, 1988, pp. 175–190.

[22] Luker, J. J., Bowersox, R. D. W., and Buter, T. A., "Influence of Curvature-Driven Favorable Pressure Gradient on Supersonic Turbulent Boundary Layer," *AIAA Journal*, Vol. 38, No. 8, 2000, pp. 1351–1359.
doi:10.2514/2.1134

[23] Smits, A. J., and Muck, K.-C., "Experimental Study of Three Shock-Wave/Turbulent Boundary Layer Interactions," *Journal of Fluid Mechanics*, Vol. 182, Sept. 1987, pp. 291–314.
doi:10.1017/S0022112087002349

[24] Colella, P., and Woodward, P. R., "The Piecewise Parabolic Method (PPM) for Gas-Dynamical Simulations," *Journal of Computational Physics*, Vol. 54, 1984, pp. 174–201.
doi:10.1016/0021-9991(84)90143-8

[25] Edwards, J. R., "A Low-Diffusion Flux-Splitting Scheme for Navier–Stokes Calculations," *Computers and Fluids*, Vol. 26, No. 6, 1997, pp. 635–659.
doi:10.1016/S0045-7930(97)00014-5

[26] Ducros, F., Ferrand, V., Nicaud, F., Weber, C., Darracq, D., Gachareiu, C., and Poinsot, T., "Large-Eddy Simulation of the Shock/Turbulence Interaction," *Journal of Computational Physics*, Vol. 152, No. 2, 1999, pp. 517–549.
doi:10.1006/jcph.1999.6238

[27] Subbareddy, P. K., and Candler, G. V., "A Fully Discrete, Kinetic Energy Consistent Finite Volume Scheme for Compressible Flows," *Journal of Computational Physics*, Vol. 228, No. 5, 2009, pp. 1347–1364.
doi:10.1016/j.jcp.2008.10.026

[28] Touber, E., and Sandham, N. D., "Large-Eddy Simulation of Low-Frequency Unsteadiness in a Turbulent Shock-Induced Separation Bubble," *Theoretical and Computational Fluid Dynamics*, Vol. 23, No. 2, 2009, pp. 79–107.
doi:10.1007/s00162-009-0103-z

[29] Boles, J. A., Choi, J.-I., Edwards, J. R., and Baurle, R. A., "Simulations of High-Speed Internal Flows Using LES/RANS Models," AIAA Paper 2009-1324, 2009.

[30] Cahuzac, A., Boudet, J., Borgnat, P., and Leveque, E., "Smoothing Algorithms for Mean Flow Extraction in Large-Eddy Simulation of Complex Turbulent Flows," *Physics of Fluids* (submitted for publication).

[31] Leveque, E., Toschi, F., Shao, L., and Bertoglio, J.-P., "A Shear Improved Smagorinsky's Model for the Large Eddy Simulation of Wall-Bounded Turbulent Flows," *Journal of Fluid Mechanics*, Vol. 570, 2007, pp. 491–502.
doi:10.1017/S0022112006003429

[32] Uribe, J. C., Jarrin, N., Prosser, R., and Laurence, D., "Development of a Two-Velocities Hybrid RANS-LES Model and Its Application to a Trailing Edge Flow," *Flow, Turbulence and Combustion*, Vol. 85, No. 2, 2010, pp. 181–197.
doi:10.1007/s10494-010-9263-6

[33] Miller, R., Dotter, J., Bowersox, R. D. W., and Buter, T. A., "Compressible Turbulence Measurements in Supersonic Boundary Layers with Favorable and Adverse Pressure Gradients," *Transitional and Turbulent Compressible Flows*, edited by E. F. Spina and C. Arakawa, Fluid Engineering Div., Vol. 224, American Society of Mechanical Engineers, New York, 1995, pp. 193–200.

[34] Fernando, E. M., and Smits, A. J., "A Supersonic Turbulent Boundary Layer in an Adverse Pressure Gradient," *Journal of Fluid Mechanics*, Vol. 211, Feb. 1990, pp. 285–307.
doi:10.1017/S0022112090001574

[35] Nikitin, N. V., Nicoud, F., Wasistho, B., Squires, K. D., and Spalart, P. R., "An Approach to Wall Modeling in Large Eddy Simulations," *Physics of Fluids*, Vol. 12, 2000, pp. 1629–1632.
doi:10.1063/1.870414

[36] Loginov, M. S., Adams, N. A., and Zheltovodov, A. A., "Large Eddy Simulation of Shock-Wave/Turbulent Boundary Layer Interaction," *Journal of Fluid Mechanics*, Vol. 565, 2006, pp. 135–169.
doi:10.1017/S0022112006000930

P. Tucker
Associate Editor